



Three-dimensionally ordered macroporous WO₃ supported Ag₃PO₄ with enhanced photocatalytic activity and durability

Yue Chang^{a,b}, Kai Yu^{b,*}, Chenxi Zhang^a, Rui Li^b, Peiyuan Zhao^a, Lan-Lan Lou^a, Shuangxi Liu^{a,c,**}

^a Institute of New Catalytic Materials Science and Key Laboratory of Advanced Energy Materials Chemistry (Ministry of Education), College of Chemistry, Nankai University, Tianjin 300071, People's Republic of China

^b College of Environmental Science and Engineering, Nankai University, Tianjin 300071, People's Republic of China

^c Collaborative Innovation Center of Chemical Science and Engineering (Tianjin), Tianjin 300072, People's Republic of China

ARTICLE INFO

Article history:

Received 27 January 2015

Received in revised form 6 April 2015

Accepted 8 April 2015

Available online 9 April 2015

Keywords:

Three-dimensionally ordered macroporous material

Ag₃PO₄/3DOM-WO₃

Visible light photodegradation

Water oxidation

Slow photon effect

ABSTRACT

Ag₃PO₄ nanoparticles were firstly deposited into the three-dimensionally ordered macroporous WO₃ (3DOM-WO₃) with different pore sizes. The resulted Ag₃PO₄/3DOM-WO₃ composites were characterized by XRD, SEM, TEM and DR UV–vis. These composite photocatalysts showed extraordinarily excellent efficiencies in the visible light degradation of organic contaminants and water splitting for oxygen evolution, which were mainly due to the synergic effect of Ag₃PO₄ and 3DOM-WO₃ as well as the periodic macroporous structure of 3DOM-WO₃. Especially, the catalyst A5W5 with Ag₃PO₄:WO₃ mass ratio of 5:5 exhibited the highest catalytic activity, and complete degradation could be achieved within 4 min for phenol and three typical dyes investigated in this work. In addition, the slow photon effect in Ag₃PO₄/3DOM-WO₃ was demonstrated, and the pore size of 3DOM-WO₃ was found to have a significant influence on the catalytic performance. The catalyst A5W5(270) showed notably higher photocatalytic activity than A5W5(150) and A5W5(420), which was mainly attributed to the exact overlap between the stop-band of 3DOM-WO₃(270) and the electronic absorption band of Ag₃PO₄/3DOM-WO₃ composite. Moreover, these composite catalysts were very stable and could be recycled ten times without any loss in photocatalytic activity for RhB degradation. More excitingly, remarkably improved activity and durability were also obtained over Ag₃PO₄/3DOM-WO₃ in water splitting for oxygen evolution. According to the XPS and HRTEM characterizations of used catalyst, the enhanced durability was mainly attributed to the effective transfer of photogenerated electrons from Ag₃PO₄ to 3DOM-WO₃.

© 2015 Elsevier B.V. All rights reserved.

1. Introduction

The visible light photocatalysis is considered as the most promising technology to solve the environmental pollution and energy shortage, which could completely decompose environmental pollutions and split water to yield hydrogen fuel by utilizing solar energy. Many attempts have been made to design and fabricate advanced visible light photocatalysts, such as energy band engineering, morphology control, nano-assembly and theoretical studies [1,2].

In the last decade, the three-dimensionally ordered macroporous (3DOM) materials, also named as inverse opals, have received much attention due to their special periodic structure coming from

the template of cubic-close-packed array of colloidal spheres [3–8]. These 3DOM materials have an open, inter-connected macropore structure and nanosized wall components, which could facilitate the mass transfer. Moreover, the periodic structure of 3DOM materials exhibited significant slow photon effect [9,10], which could forbid the propagation of light with certain wavelengths through the material and resulted in a stop-band reflection. The slow photon effect could increase the photon-matter interaction length and enhance the light energy conversion efficiency.

The enhancement of light harvesting efficiency by inverse opals was demonstrated by Mallouk and co-workers [11,12] in a dye-sensitized solar cell through coupling a TiO₂ photonic crystal layer to a conventional TiO₂ film. After that, a series of 3DOM semiconductor materials were prepared and used as photocatalysts, including TiO₂ [11–24], Bi₂WO₆ [25], InVO₄ [26–28], WO₃ [29,30], BiVO₄ [31,32] and SnO₂ [33,34]. Su and co-workers [13–15] prepared 3DOM TiO₂ with different pore diameters and studied the influence of the photonic structure on the activity of

* Corresponding author. Tel.: +86 22 23509005; fax: +86 22 23509005.

** Corresponding author. Tel.: +86 22 23509005; fax: +86 22 23509005.

E-mail addresses: kaiyu@nankai.edu.cn (K. Yu), sxliu@nankai.edu.cn (S. Liu).

TiO₂ for the photodegradation of Rhodamine B (RhB). Qi et al. [16] reported Ti³⁺ doped TiO₂ inverse opals and these photocatalysts showed notably enhanced visible light harvesting ability. Dai and co-workers [26–28] reported 3DOM InVO₄ and noble metal loaded 3DOM InVO₄-BiVO₄ catalysts, which performed excellently for MB and RhB degradation under visible light irradiation. These reported 3DOM semiconductor materials show an attractive prospect in the photocatalysis field, however, the related studies are still extremely lack. Particularly, the composite photocatalysts based on 3DOM materials were seldom reported till now [28,32–34].

Silver orthophosphate (Ag₃PO₄), as a very efficient visible-light-driven catalyst [35–41], can oxidize water to release oxygen as well as degrade organic contaminants under visible light irradiation, however, it always suffered from stability issue [42–45]. In this work, a series of 3DOM-WO₃ materials with different pore sizes were synthesized through a PMMA colloidal crystal template method, and the Ag₃PO₄ nanoparticles were firstly deposited in the macropores of 3DOM-WO₃. These novel Ag₃PO₄/3DOM-WO₃ composites were evaluated in the visible light degradation of organic contaminants and water oxidation. An amazing increase in photocatalytic efficiency was expected over these Ag₃PO₄/3DOM-WO₃ composites due to the effective separation of electron-hole pairs, facile mass transfer and slow photon effect derived from inverse opals. Moreover, the advantages of these photocatalysts were also reflected in the notably enhanced stability attributed to the effective transfer of electrons and holes.

2. Experimental

2.1. Materials

Methyl methacrylate (MMA) stabilized with 30 ppm MEHQ, silver nitrate (AgNO₃) and quartz sand were purchased from Aladdin. Potassium persulfate (K₂S₂O₈), cetyltrimethylammonium bromide (CTAB), methanol and disodium hydrogen phosphate (Na₂HPO₄) were obtained from Sinopharm Chemical Reagent Co., Ltd. 2,2-Azobis(2-methylpropionamide) dihydrochloride (AIBA) and ammonium metatungstate hydrate ((NH₄)₆H₂W₁₂O₄₀·xH₂O) were purchased from Energy Chemical and Beijing HWRK Chem Co., Ltd., respectively. Sodium tungstate dihydrate (Na₂WO₄·2H₂O), ammonium chloride (NH₄Cl), dimethyl sulfoxide (DMSO), phenol, bisphenol A (BPA), malachite green (MG), methylene blue (MB) and RhB were obtained from Tianjin Heowns Biochemical Technology

Co., Ltd. All of the reagents were analytical grade and all aqueous solutions were prepared with deionized water.

2.2. Characterization

A JEOL JSM-7500F field-emission scanning electron microscope (SEM) was used in order to observe the morphology of photocatalysts. The high-resolution transmission electron microscopy (HRTEM) images were taken using a Philips Tecnai G2 F30 instrument. The X-ray powder diffraction (XRD) patterns of the samples were acquired using Bruker D8 X-ray diffractometer with Cu Kα radiation at a scan rate of 0.01° s⁻¹, the operation voltage and current respectively remained 40 kV and 40 mA over 2θ range from 10° to 80°. Diffuse-reflectance UV-vis (DR UV-vis) spectra were obtained on a Shimadzu UV-2550 spectrophotometer with an integral sphere employing BaSO₄ as a reference in the measurement range from 220 nm to 800 nm. N₂ sorption analysis was carried out at 77 K on a Micromeritics TriStar 3000 apparatus and the surface areas were determined by BET method. X-ray photoelectron spectroscopy (XPS) spectra were recorded on a Kratos Axis Ultra DLD with a AlKα X-ray source. The UV-vis absorption spectra of organic dyes in water were determined on a Shimadzu UV-2550 spectrophotometer. High-performance liquid chromatography (HPLC) analysis was carried out on an Agilent 1200 series HPLC instrument equipped with an Agilent XDB-C18 column and a UV detector (270 nm for phenol and 224 nm for BPA, respectively). The mobile phase was a mixture of acetonitrile and water (50/50, v/v), and was pumped at a flow rate of 0.7 mL min⁻¹. The online gas chromatography (GC) analysis in photocatalytic oxygen evolution experiments was performed on a FL9790II gas chromatograph equipped with a thermal conductive detector (TCD) and a carbon molecular sieve column, using argon as the carrier gas.

2.3. Synthesis of WO₃

2.3.1. Synthesis of 3DOM-WO₃ with different pore sizes

Three kinds of PMMA microspheres with average diameters of ca. 150 nm, 270 nm and 420 nm, respectively, were synthesized from MMA using a soap-free emulsion polymerization method. The details about the synthesis and characterization of PMMA microspheres are given in Supplementary materials. The well-arranged PMMA colloidal crystal templates were fabricated by centrifugation.

The 3DOM-WO₃ materials were synthesized according to the literatures [29,30]. A desired amount of (NH₄)₆H₂W₁₂O₄₀ was dissolved in a mixture solution of deionized water (1.6 mL) and methanol (1 mL), thus a precursor solution was obtained with the total tungstate ion concentration of 2.5 M. The PMMA colloidal crystal template was soaked in the prepared precursor solution for 3 h. The redundant precursor solution was removed from the impregnated PMMA template via filtration. The sample was dried in a vacuum oven at 35 °C for 4 h and mixed with quartz sand (8–16 mesh). The mixed sample was calcined in a muffle furnace at 100 °C for 0.5 h, followed by a ramp of 1 °C/min to 300 °C and held for 3 h to remove the PMMA template. The temperature was continuously raised up 390 °C and held for 3 h before cooling down to room temperature. The as-synthesized 3DOM-WO₃ materials were marked as 3DOM-WO₃(150), 3DOM-WO₃(270) and 3DOM-WO₃(420), respectively.

2.3.2. Synthesis of rodlike WO₃

Na₂WO₄·2H₂O (0.003 mol) and NH₄Cl (0.01 mol) were dissolved in 60 mL and 20 mL of deionized water, respectively. The above two solutions were mixed in ultrasonic water bath for 1 h. The mixture was poured into a 100 mL Teflon-lined stainless steel autoclave and kept at 180 °C for 48 h. After cooling down to room temperature,

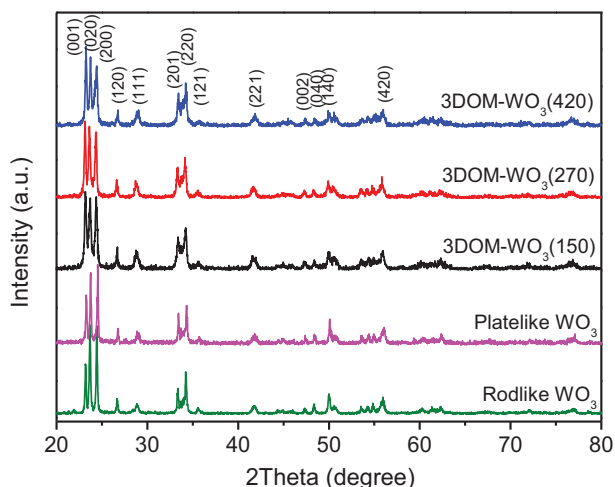


Fig. 1. Powder XRD patterns of 3DOM-WO₃, rodlike WO₃ and platelike WO₃.

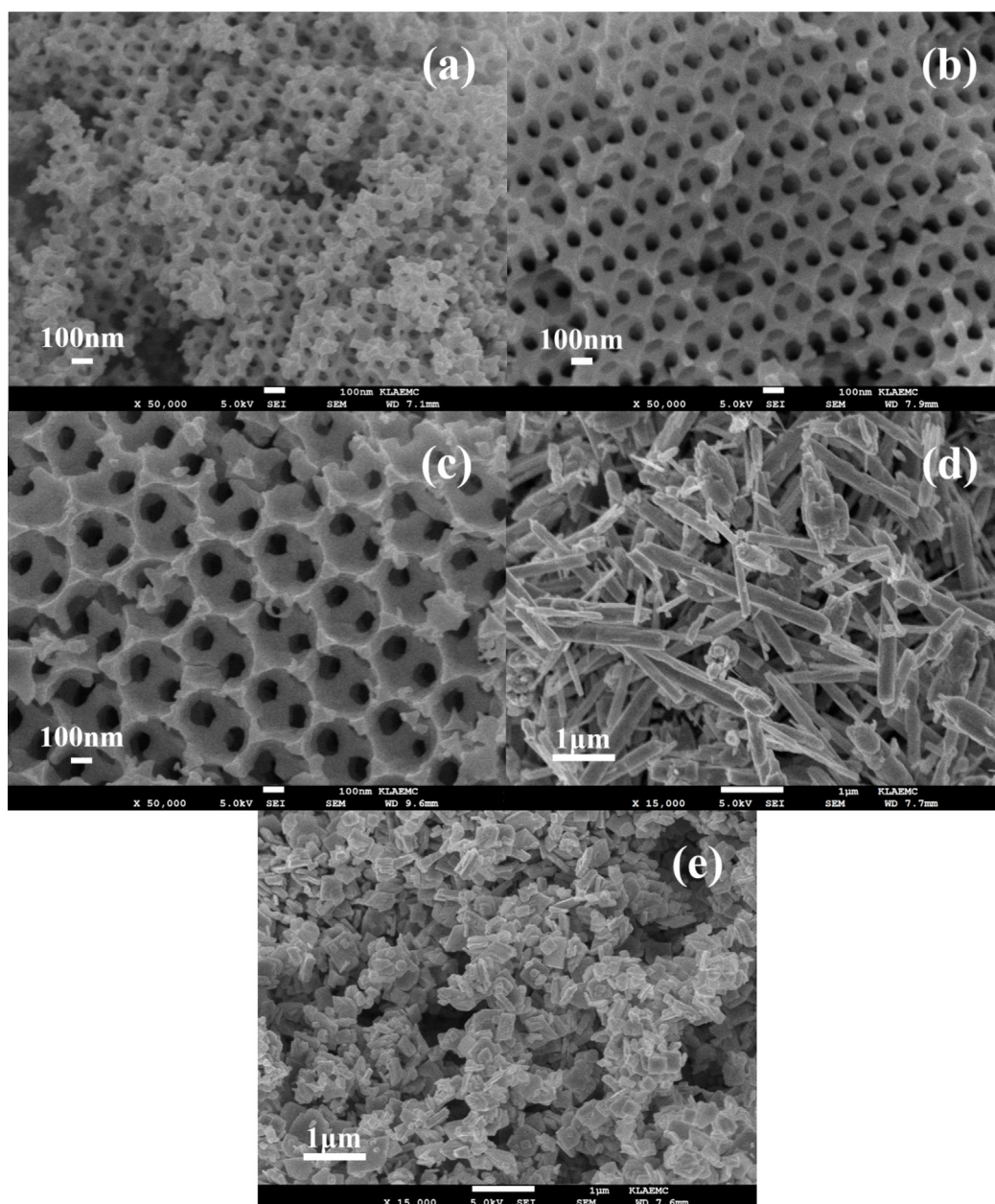


Fig. 2. SEM micrographs of 3DOM-WO₃ (a–c), Rodlike WO₃ (d) and Platelike WO₃ (e).

the precipitate was collected by centrifugation and washed with distilled water, then dried in vacuum at 65 °C for 12 h. The dried sample was calcined in air at 500 °C for 2 h with a heating rate of 1 °C/min and then rodlike WO₃ was obtained.

2.3.3. Synthesis of platelike WO₃

Na₂WO₄·2H₂O (3.0 g) and CTAB (0.005 g) were dissolved in 10 mL of deionized water. 3 mL of the above solution was added

drop wise into 5 mL of HCl solution (3.0 M). The mixture was stirred for 30 min at room temperature and then heated to 100 °C for 24 h in the air oven. The precipitate was collected by centrifugation, washed with deionized water and acetone for several times. The sample was calcined in air at 300 °C for 3 h with a heating rate of 1 °C/min and then platelike WO₃ was obtained.

2.4. Synthesis of Ag₃PO₄/3DOM-WO₃ composite photocatalysts

Ag₃PO₄/3DOM-WO₃ composite photocatalysts were synthesized through a deposition–precipitation method, and the typical synthesis procedure was carried out as follows. A certain amount of AgNO₃ was added into a mixture solution of deionized water (12.5 mL) and DMSO (25 mL) at room temperature under stirring until completely dissolved. 3DOM-WO₃ was dispersed into this solution under continuous stirring for 15 min, followed by the dropping of Na₂HPO₄ aqueous solution (0.15 M). Table 1 lists the composition of various reaction solutions. After stirring for 30 min,

Table 1

The synthesis conditions of Ag₃PO₄/3DOM-WO₃ photocatalysts.

Sample	Mass ratio (Ag ₃ PO ₄ :WO ₃)	Amount of AgNO ₃ (g)	Amount of 3DOM-WO ₃ (g)	Volume of Na ₂ HPO ₄ solution (mL)
A3W7	3:7	0.06	0.064	3.0
A5W5	5:5	0.10	0.046	5.0
A7W3	7:3	0.14	0.027	7.0

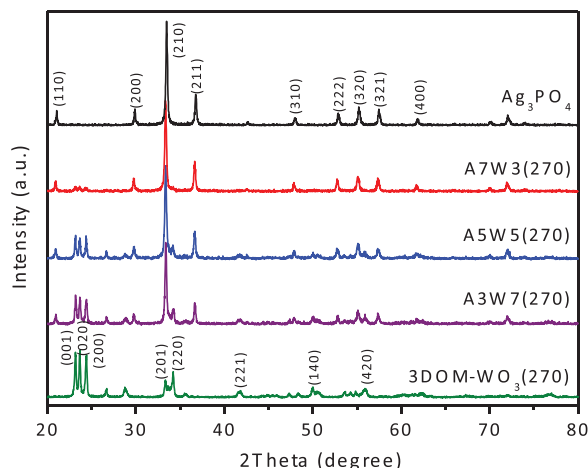


Fig. 3. Powder XRD patterns of Ag_3PO_4 , 3DOM- WO_3 (270) and Ag_3PO_4 /3DOM- WO_3 (270) composites.

the obtained precipitate was collected by centrifugation, washed with ethanol and deionized water for several times, and dried at 65 °C for 12 h. According to the mass ratio of Ag_3PO_4 to WO_3 , the as-synthesized Ag_3PO_4 /3DOM- WO_3 photocatalysts were marked as A3W7(x), A5W5(x), and A7W3(x), respectively, in which $x = 150$, 270, or 420.

For comparison, Ag_3PO_4 was also combined with rodlike WO_3 and platelike WO_3 through the deposition–precipitation method under the same conditions, and the obtained photocatalysts were marked as Ag_3PO_4 /Rod- WO_3 and Ag_3PO_4 /Plate- WO_3 , respectively. Moreover, a pure Ag_3PO_4 catalyst was prepared at the same conditions in the absence of WO_3 .

2.5. Photocatalytic degradation of organic contaminants

In order to determine the photocatalytic activity of the photocatalysts, the degradation efficiencies of organic contaminants including RhB, MB, MG, phenol and BPA were used as an index. In a typical process, 50 mL of organic contaminant solution and 50 mg of photocatalyst sample were mixed and magnetically stirred in the 200 mL quartz photo reactor in the dark for 30 min to establish an adsorption–desorption equilibrium between organic contaminant and catalyst. Then, the suspended solution was irradiated by a 210 W Xe lamp with a cutoff filter of 420 nm. After the photodegradation, the catalyst was separated from the reaction solution by centrifugation, thoroughly washed, and then reused in the following run. The concentration of organic contaminant was measured by the maximum of absorbance in UV–vis absorption spectra and HPLC. The corresponding UV–vis spectra and HPLC profiles of these organic contaminants under photocatalytic process are described in Supplementary materials.

2.6. Photocatalytic oxygen evolution experiments

The photocatalytic oxygen evolution experiments were performed in a 250 mL quartz flask at room temperature and using a 300 W Xe lamp with a cutoff filter of 420 nm as light source. In a typical process, 0.3 g of photocatalyst was dispersed in 150 mL of deionized water under stirring, and AgNO_3 (0.51 g) was added into the mixture as sacrificial reagent. The system was thoroughly degassed by evacuation and then the suspension was irradiated by visible light. The evolved oxygen was analyzed by online GC.

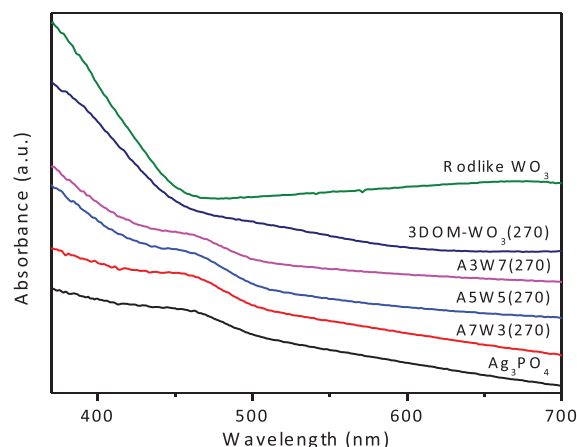


Fig. 4. DR UV–vis spectra of Ag_3PO_4 , 3DOM- WO_3 (270) and Ag_3PO_4 /3DOM- WO_3 (270) composites.

3. Results and discussion

3.1. Characterization of the 3DOM- WO_3 materials

The as-synthesized 3DOM- WO_3 , rodlike WO_3 and platelike WO_3 were characterized by XRD and SEM. As shown in Fig. 1, the characteristic diffraction peaks of (001), (020), (200), (120), (111), (201), (220), (121), (221), (002), (040), (140) and (420) can be perfectly indexed as the orthorhombic phase WO_3 (JCPDS no. 20-1324). The SEM images of 3DOM- WO_3 , rodlike WO_3 and platelike WO_3 are shown in Fig. 2. It could be seen from Fig. 2(a–c) that a well-ordered inverse opal structure was appeared in as-synthesized 3DOM- WO_3 materials. The average pore diameters of 3DOM- WO_3 (150), 3DOM- WO_3 (270) and 3DOM- WO_3 (420) were about 95 nm, 224 nm and 360 nm, respectively, which showed a shrinkage in the range of 14–36% compared with the PMMA microspheres. The rodlike WO_3 exhibited a length of 1–3 μm and a diameter of ~ 250 nm, meanwhile the platelike WO_3 had a width of 200–500 nm and a thickness of ~ 100 nm.

3.2. Characterization of the Ag_3PO_4 /3DOM- WO_3 composites

The Ag_3PO_4 /3DOM- WO_3 composites were characterized by XRD, SEM, TEM, DR UV–vis and N_2 sorption. Fig. 3 shows the XRD patterns of Ag_3PO_4 /3DOM- WO_3 (270) with different mass ratios of Ag_3PO_4 to WO_3 . With the increase of Ag_3PO_4 : WO_3 mass ratio from 3:7 to 7:3, the intensities of Ag_3PO_4 diffraction peaks increased evidently, while the intensities of WO_3 diffraction peaks gradually decreased. Moreover, no additional diffraction peaks were observed in the XRD patterns of Ag_3PO_4 /3DOM- WO_3 (270) composites except for the characteristic peaks of Ag_3PO_4 and WO_3 .

Fig. 4 describes the DR UV–vis spectra of Ag_3PO_4 , 3DOM- WO_3 (270), A3W7(270), A5W5(270), A7W3(270) and rodlike WO_3 . It could be found that the optical absorption edge was estimated to be ~ 450 nm for WO_3 and ~ 500 nm for Ag_3PO_4 , respectively. With the increase of Ag_3PO_4 content in Ag_3PO_4 /3DOM- WO_3 composites, the absorption edge was observed to gradually move to longer wavelength. Moreover, compared with rodlike WO_3 , 3DOM- WO_3 (270) exhibited a notably enhanced optical absorbance in the wavelengths of 460–550 nm, which was mainly attributed to the slow photon effect of 3DOM materials.

The morphologies of as-synthesized Ag_3PO_4 /3DOM- WO_3 composites were characterized by SEM and TEM. Fig. 5 shows the typical SEM images of Ag_3PO_4 and A5W5 composites with different pore sizes. It could be found that the nano Ag_3PO_4 catalyst was sphere-like with a diameter of 40–100 nm. For the Ag_3PO_4 /3DOM- WO_3

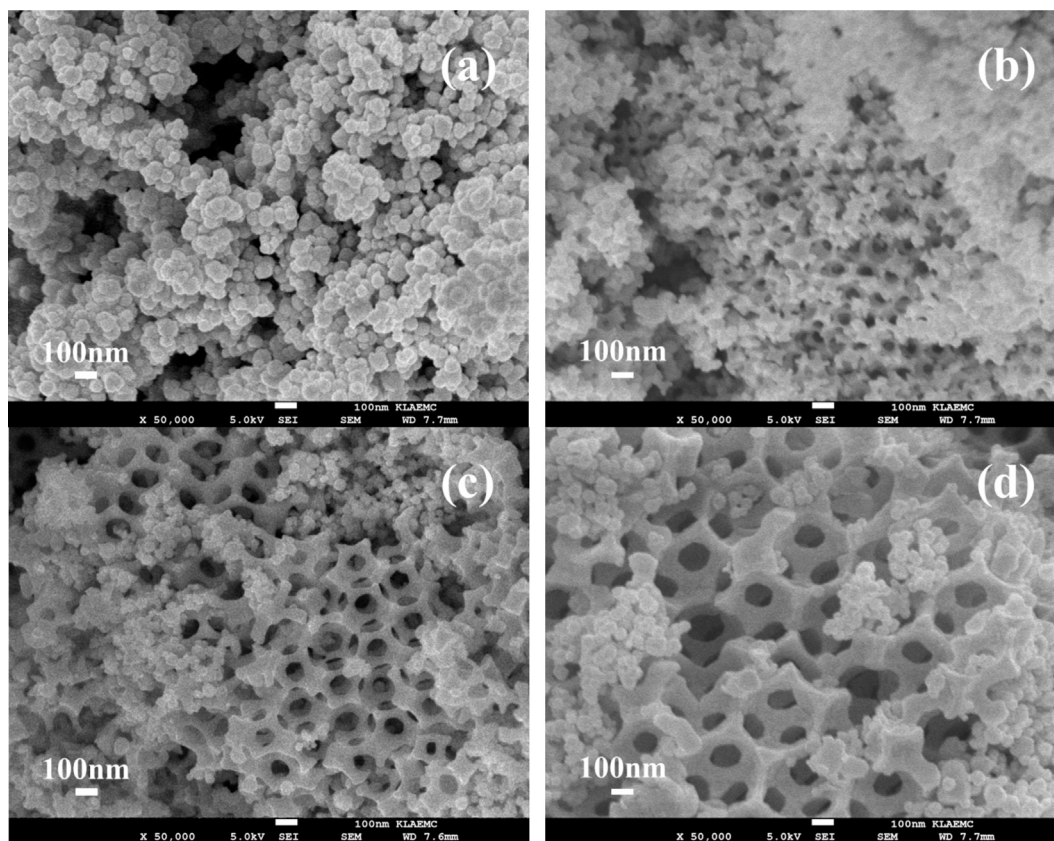


Fig. 5. SEM micrographs of photocatalysts Ag_3PO_4 (a), A5W5(150) (b), A5W5(270) (c) and A5W5(420) (d).

composites, as shown in Fig. 5(b–d), the Ag_3PO_4 nano particles with a diameter of 20–50 nm were dispersed into the macropores of 3DOM- WO_3 . Moreover, the well-ordered periodic macroporous structure of 3DOM- WO_3 was maintained in Ag_3PO_4 /3DOM- WO_3 composites. The TEM images of 3DOM- WO_3 (270) and A5W5(270) (as shown in Fig. 6) also clearly proved that the Ag_3PO_4 particles were deposited in the macropores of 3DOM- WO_3 .

The 3DOM- WO_3 and A5W5 catalysts were characterized by N_2 sorption and the corresponding textural parameters are listed in Table 2. It was shown that the BET surface areas of as-

synthesized 3DOM- WO_3 and A5W5 composites were in the range of $8.7\text{--}16.9\text{ m}^2\text{ g}^{-1}$. Among these samples, 3DOM- WO_3 (150) and A5W5(150) exhibited relatively higher BET surface areas due to the smaller pore diameter.

3.3. Effect of Ag_3PO_4 : WO_3 mass ratio on the photocatalytic activity

The photocatalytic activity of Ag_3PO_4 /3DOM- WO_3 (270) composites with different Ag_3PO_4 : WO_3 mass ratios was evaluated

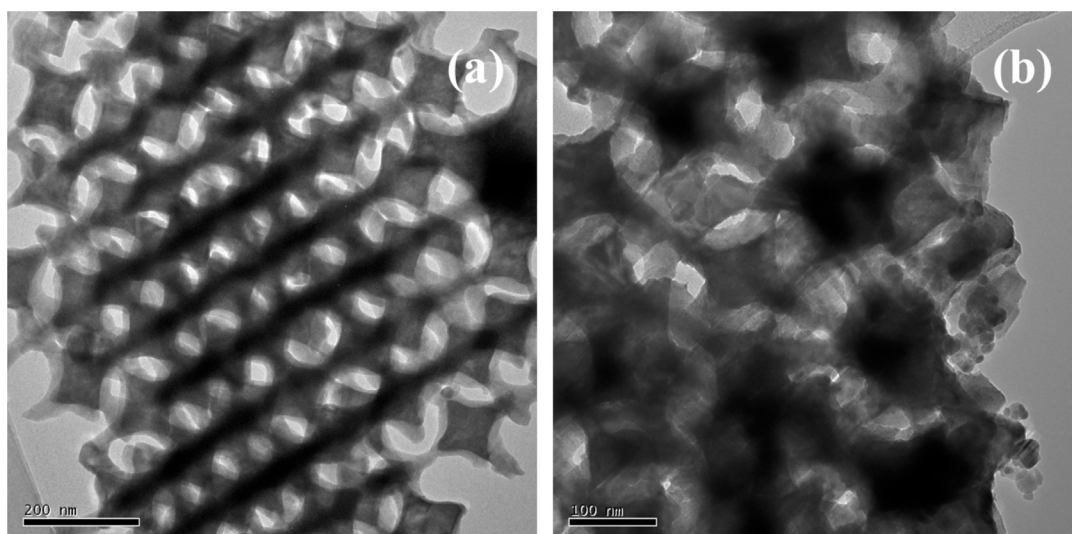


Fig. 6. TEM micrographs of 3DOM- WO_3 (270) (a) and A5W5(270) (b).

Table 2
The BET surface areas of 3DOM-WO₃ and Ag₃PO₄/3DOM-WO₃ composites.

Sample	S _{BET} (m ² g ⁻¹)
3DOM-WO ₃ (150)	16.9
A5W5(150)	10.5
3DOM-WO ₃ (270)	11.1
A5W5(270)	9.6
3DOM-WO ₃ (420)	10.7
A5W5(420)	8.7

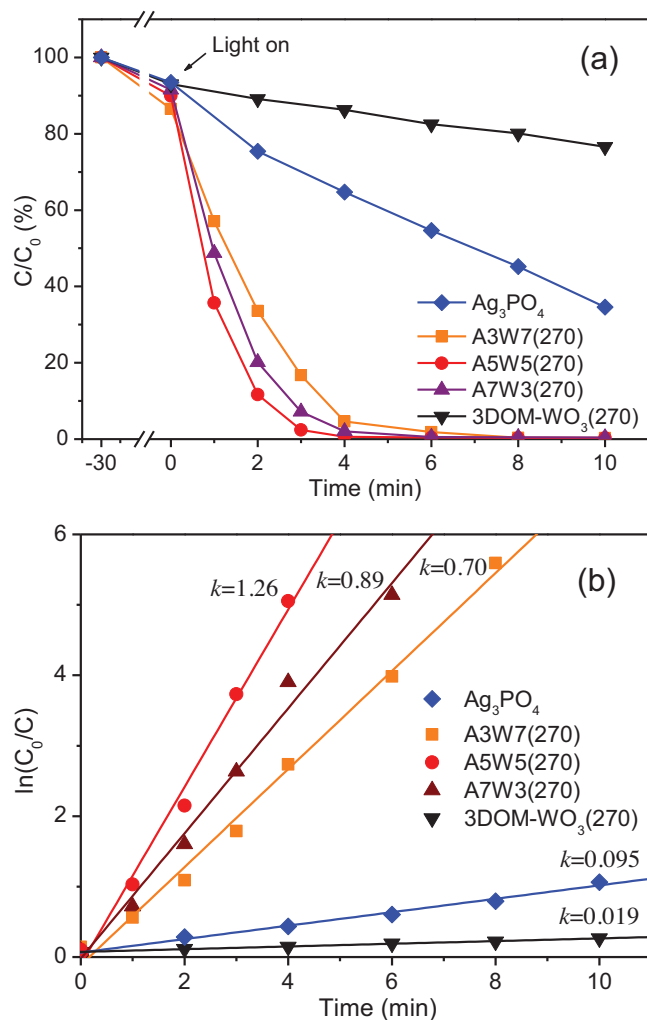


Fig. 7. Photodegradation of RhB catalyzed by Ag₃PO₄, 3DOM-WO₃(270) and Ag₃PO₄/3DOM-WO₃(270) with different Ag₃PO₄:WO₃ mass ratios.

by the degradation of RhB (10 ppm) under visible light irradiation. For comparison, pure Ag₃PO₄ and 3DOM-WO₃(270) were also employed. As shown in Fig. 7(a), all the three Ag₃PO₄/3DOM-WO₃(270) composites exhibited notably higher photocatalytic activity than Ag₃PO₄ and 3DOM-WO₃(270). After 6 min irradiation, nearly 100% of RhB could be degraded by Ag₃PO₄/3DOM-WO₃ composites, while only 45% and 18% of RhB could be degraded by pure Ag₃PO₄ and 3DOM-WO₃(270), respectively. It meant that the remarkable synergic effect of Ag₃PO₄ and 3DOM-WO₃ existed in Ag₃PO₄/3DOM-WO₃ composites. As described in Fig. 8, the electron-hole pairs were generated on the surface of Ag₃PO₄ and 3DOM-WO₃ under visible light irradiation. When 3DOM-WO₃ and Ag₃PO₄ were combined, the photogenerated electrons would move from the conduction band of Ag₃PO₄ to that of 3DOM-WO₃, and the photogenerated holes moved from the valence band of 3DOM-

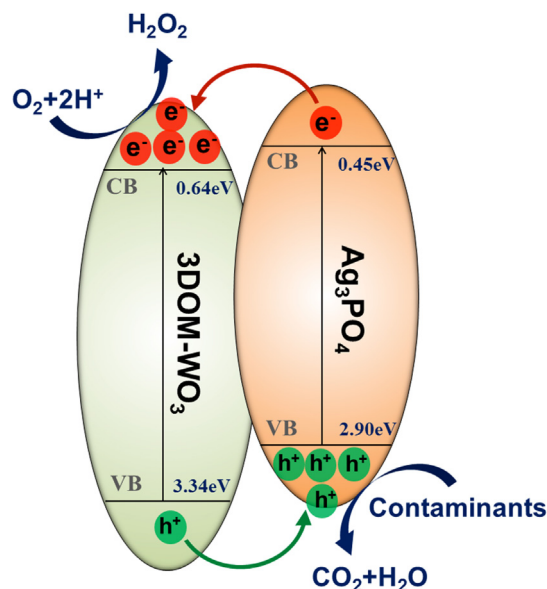


Fig. 8. Schematic representation for the enhanced photocatalytic efficiency of Ag₃PO₄/3DOM-WO₃ composites.

WO₃ to that of Ag₃PO₄. Thus the organic contaminants could be directly oxidized by the holes on Ag₃PO₄ surface [37,46,47], while the electrons would be consumed through a multi-electron reaction with oxygen ($O_2 + 2H^+ + 2e^- \rightarrow H_2O_2$) [48]. In other words, the combination of 3DOM-WO₃ and Ag₃PO₄ could lead to the effective separation of photogenerated electron-hole pairs and consequently improve the photocatalytic performance.

It could be also found from Fig. 7(a) that the mass ratio of Ag₃PO₄:WO₃ had an obvious influence on the catalytic performance of Ag₃PO₄/3DOM-WO₃ catalysts for the photodegradation of RhB. Compared with A3W7(270) and A7W3(270), the catalyst of A5W5(270) exhibited the highest catalytic activity and could decompose 10 ppm of RhB (degradation efficiency >99%) in 4 min under visible light irradiation. While for the catalysts of A3W7(270) and A7W3(270), 8 min and 6 min were required, respectively, under the same reaction conditions. These results can also be confirmed by the kinetic data curves shown in Fig. 7(b). It was observed that the photocatalytic degradation of RhB follows the pseudo first-order reaction. The rate constant k is calculated by the Langmuir-Hinshelwood model [$\ln(C_0/C) = kt$]. The kinetic rate constants on A3W7(270), A5W5(270) and A7W3(270) were about 0.70 min⁻¹, 1.26 min⁻¹ and 0.89 min⁻¹, respectively, which were significantly higher than those over pure Ag₃PO₄ (0.095 min⁻¹) and 3DOM-WO₃ (0.019 min⁻¹). The results suggest that suitable mass ratio of Ag₃PO₄ to 3DOM-WO₃ could improve the catalytic activity of the composite photocatalysts. In current catalytic system, the catalyst A5W5 exhibited the highest catalytic performance.

3.4. Effect of 3DOM-WO₃ pore size on the photocatalytic activity

To investigate the influence of macropore diameter on photocatalytic activity of Ag₃PO₄/3DOM-WO₃ composites, A5W5(150), A5W5(270) and A5W5(420) were evaluated in the degradation of RhB (10 ppm) under visible light irradiation. In addition, three 3DOM-WO₃ samples, Ag₃PO₄/Rod-WO₃ and Ag₃PO₄/Plate-WO₃ were also employed for comparison. The Ag₃PO₄:WO₃ mass ratio in all these composite photocatalysts was fixed as 5:5. Fig. 9 depicts the degradation and kinetic data curves of RhB catalyzed by these photocatalysts.

As shown in Fig. 9, all the Ag₃PO₄/3DOM-WO₃ catalysts exhibited notably higher photocatalytic activities than Ag₃PO₄/Rod-WO₃

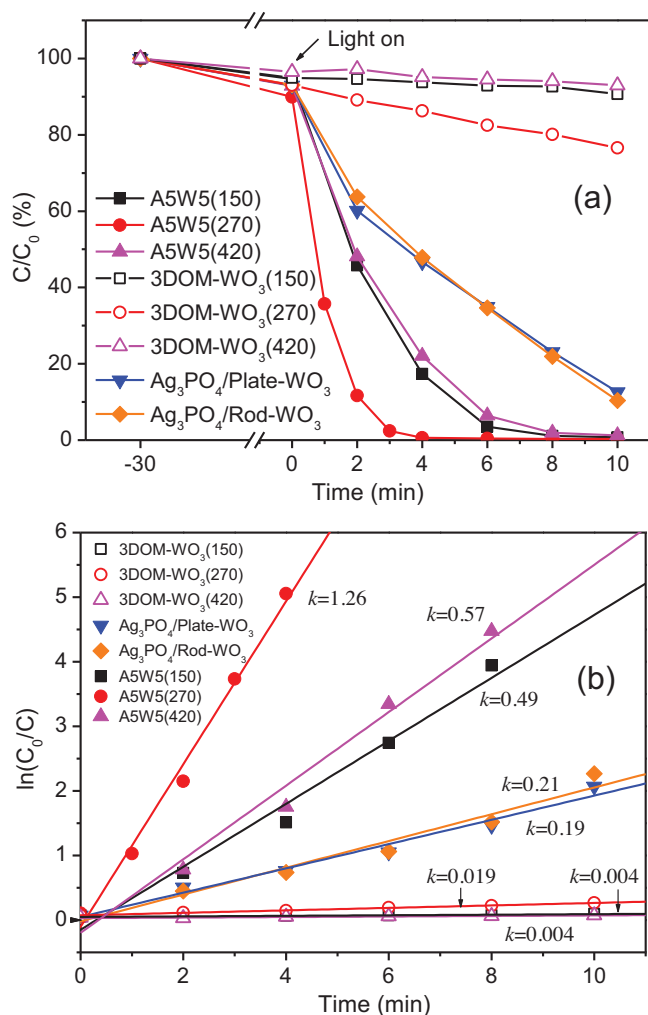


Fig. 9. Photodegradation of RhB catalyzed by Ag₃PO₄/Rod-WO₃, Ag₃PO₄/Plate-WO₃, 3DOM-WO₃ and A5W5(*x*).

and Ag₃PO₄/Plate-WO₃ catalysts. More than 97% of RhB could be degraded by A5W5 in 6 min, while for the latter two catalysts, the degradation efficiency of RhB only achieved about 67% under the same reaction conditions. This meant that the macroporous structure of inverse opals could remarkably improve the photo-

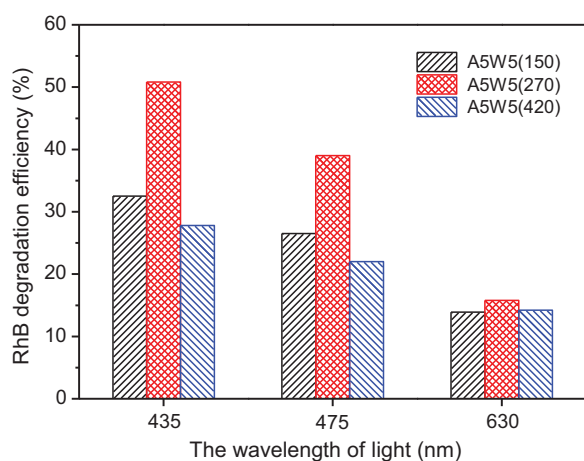


Fig. 10. Photodegradation of RhB catalyzed by A5W5(*x*) composites under the certain wavelength light irradiation.

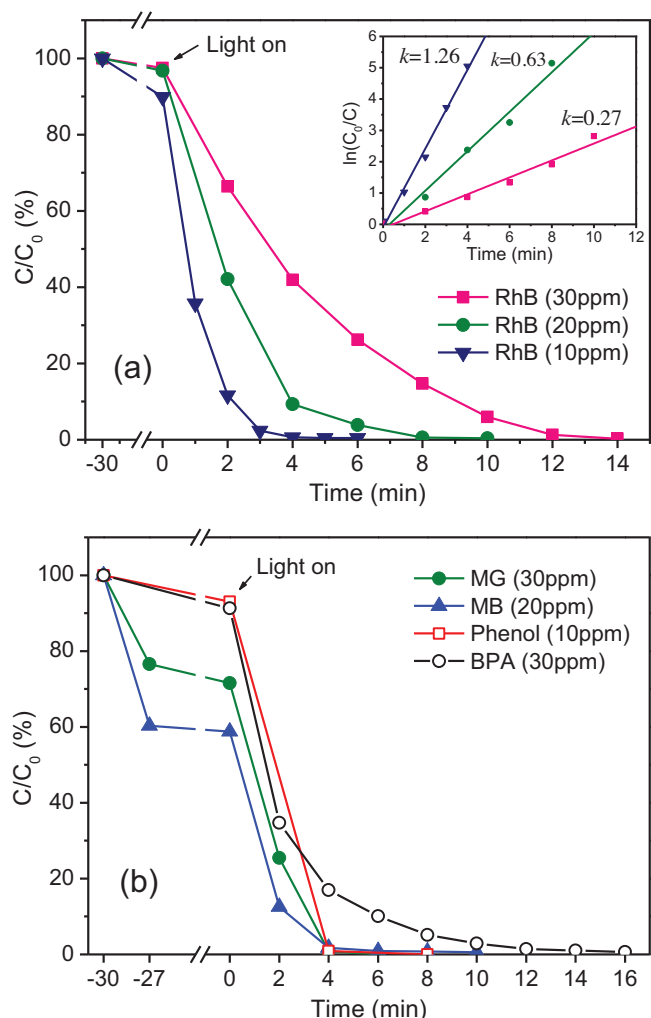


Fig. 11. Photodegradation of organic contaminants under visible light irradiation catalyzed by A5W5(270).

catalytic activity of Ag₃PO₄/3DOM-WO₃ catalysts, which may be explained by the following reasons. Firstly, the ordered macroporous structure of inverse opals could facilitate the mass transfer of pollutant molecules [18,20,49,50]. Secondly, the nanosized wall of 3DOM-WO₃ could shorten the diffusion length of photogenerated electron-hole pairs and prevent their recombination. Finally and most importantly, the slow photon effect of inverse opals could obviously increase the photon-matter interaction length and consequently enhance the light energy conversion efficiency.

To study the influence of slow photon effect in Ag₃PO₄/3DOM-WO₃ catalysts, the catalytic performance of A5W5(150), A5W5(270) and A5W5(420) was compared in this section. It could be found from Fig. 9, A5W5(270) exhibited the most excellent catalytic efficiency in the photodegradation of RhB compared with A5W5(150) and A5W5(420). The calculated rate constant k on A5W5(270) was 1.26 min^{-1} , which was notably higher than those for A5W5(150) (0.49 min^{-1}) and A5W5(420) (0.57 min^{-1}). Similarly, 3DOM-WO₃(270) showed obviously improved photocatalytic activity than 3DOM-WO₃(150) and 3DOM-WO₃(420), even though it possessed the middling BET surface area. According to the modified Bragg's law (as described in Eq. (1)), the stop-band of inverse opals can be fixed to a given wavelength [30,51]. In this equation, λ_{max} is the wavelength of stop-band, D is the pore diameter of the inverse opal, n_{WO_3} and n_{water} are the refractive index of WO₃ and water, respectively, f is

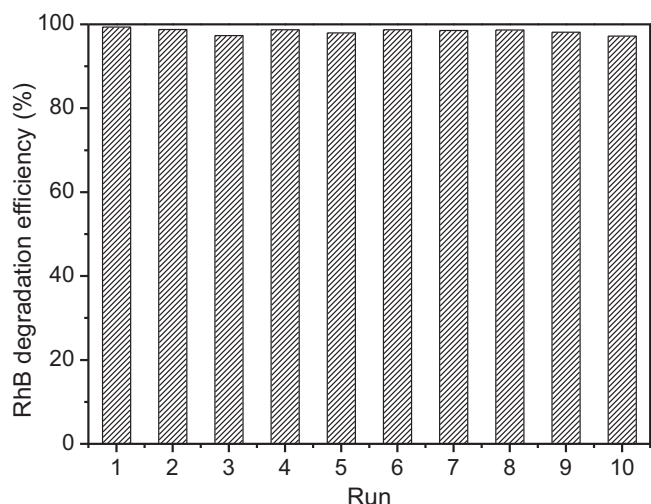


Fig. 12. Recycling tests of A5W5(270) for the degradation of RhB under visible light irradiation.

the WO_3 phase volume percentage (generally $f=0.26$), and θ is the incident angle of light (normally $\theta=0^\circ$). Based on this equation, the calculated photonic stop-band of 3DOM- WO_3 (270) was about 490 nm ($D=224$ nm), while for 3DOM- WO_3 (150) ($D=95$ nm) and 3DOM- WO_3 (420) ($D=360$ nm), the stop-bands were about 208 nm and 790 nm, respectively. These calculated stop-bands of

3DOM- WO_3 were consistent with the detected results through DR UV-vis spectroscopy (as shown in Fig. S2).

$$\lambda_{\max} = 2\sqrt{\frac{2}{3}}D\sqrt{n_{\text{WO}_3}^2f + n_{\text{water}}^2(1-f) - \sin^2\theta} \quad (1)$$

It could be found from Fig. 4, the $\text{Ag}_3\text{PO}_4/3\text{DOM-}\text{WO}_3$ catalysts exhibited a notable absorbance in the range of 420–500 nm, which was exactly overlapped with the stop-band of 3DOM- WO_3 (270). The slow photons were limited in the matrix via multiple scattering and diffraction, which leads to much stronger interaction between light and photocatalyst. However, the stop-band of 3DOM- WO_3 (420) was too large to be utilized and the stop-band of 3DOM- WO_3 (150) was in the range of ultraviolet region. Therefore, the catalyst of A5W5(270) exhibited the best activity in the visible light degradation of RhB as compared with A5W5(150) and A5W5(420). In order to further confirm the influence of slow photon effect in $\text{Ag}_3\text{PO}_4/3\text{DOM-}\text{WO}_3$ catalysts, the RhB photodegradation reactions over A5W5 composites with different pore sizes were carried out under the certain wavelength light irradiation (210 W Xe lamp equipped with short-wavelength pass filter of 435 nm, 475 nm, or 630 nm). The RhB degradation efficiencies were detected under visible light irradiation for 4 min and the results are shown in Fig. 10. It could be found that A5W5(270) exhibited notably higher catalytic activity than A5W5(150) and A5W5(420) when the wavelength of light was 435 nm or 475 nm. However, the three catalysts exhibited comparable catalytic performance when the light wavelength was 630 nm. Taking into account the stop-bands of 3DOM- WO_3 materials, it could be concluded that the slow photon effect of inverse opal could significantly improve

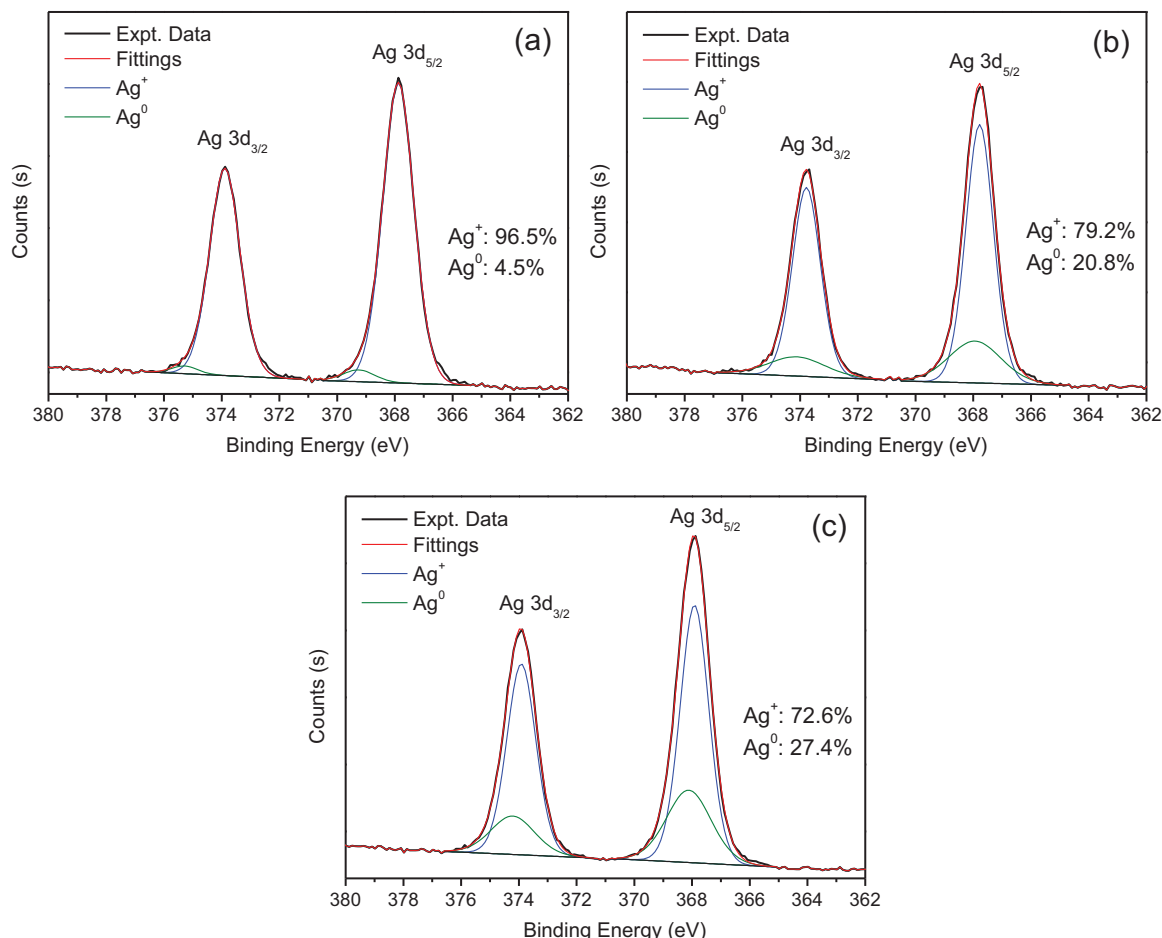


Fig. 13. High-resolution $\text{Ag}3\text{d}$ XPS spectra of A5W5(270) used one time (a) and ten times (b), and Ag_3PO_4 used one time (c) for RhB photodegradation.

the catalytic performance of photocatalyst when the photonic stop-band of inverse opal was overlapped with the electronic absorption band of semiconductor. The improved catalytic activity over 3DOM-WO₃(270) compared with 3DOM-WO₃(150) and 3DOM-WO₃(420) could also be attributed to this reason.

3.5. Photocatalytic degradation of organic contaminants

In the following catalytic tests, the most active catalyst, A5W5(270), was selected to decompose various organic contaminants with different initial concentrations. Firstly, the RhB solutions with different initial concentrations (10 ppm, 20 ppm and 30 ppm) were degraded by A5W5(270). As shown in Fig. 11(a), faster degradation could be observed as the initial RhB concentration was relatively low. The time required for complete degradation raised from 4 min to 8 min then to 14 min as the initial concentration of RhB was 10 ppm, 20 ppm and 30 ppm, respectively. The pseudo first order rate constants were about 0.63 min⁻¹ and 0.27 min⁻¹ for 20 ppm and 30 ppm RhB, respectively.

In order to gain better insight into the catalytic performance of the Ag₃PO₄/3DOM-WO₃ composites, phenol, BPA, MG and MB were also employed as target pollutants. As depicted in Fig. 11(b), MB (20 ppm), MG (30 ppm) and phenol (10 ppm) could be completely

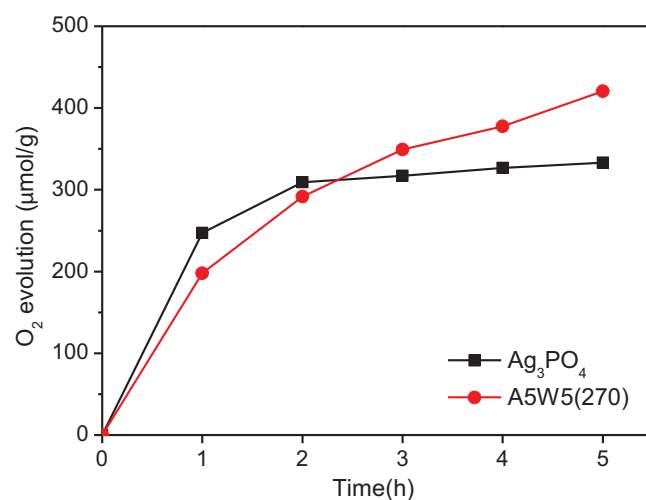


Fig. 14. Oxygen evolution from photocatalytic water splitting with Ag₃PO₄ and A5W5(270).

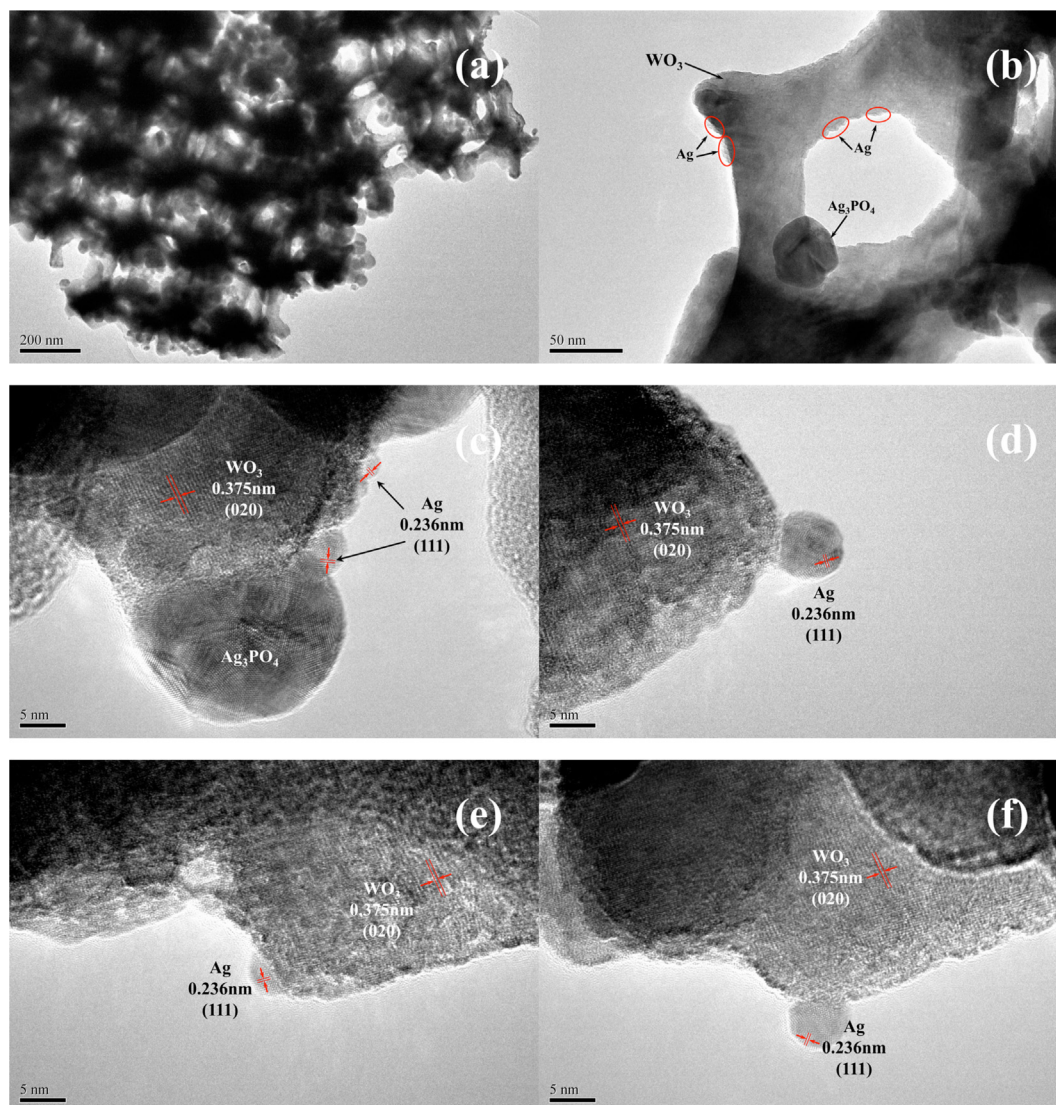


Fig. 15. TEM micrographs of A5W5(270) after photocatalytic water oxidation reaction.

degraded under visible light irradiation for 4 min. Meanwhile, the degradation of BPA (30 ppm) could be finished within 16 min. It is noteworthy that these results are significantly better than those previously reported [37,44,52–56], indicating that the present $\text{Ag}_3\text{PO}_4/\text{3DOM-WO}_3$ photocatalysts were highly efficient in the visible light degradation of organic contaminants.

3.6. Photocatalytic stability of the $\text{Ag}_3\text{PO}_4/\text{3DOM-WO}_3$ composites

The stability of as-synthesized $\text{Ag}_3\text{PO}_4/\text{3DOM-WO}_3$ photocatalysts was investigated in this section. Fig. 12 shows the degradation efficiencies of RhB in ten consecutive applications with A5W5(270) as the catalyst under visible light irradiation for 4 min. To our delight, the catalyst A5W5(270) could be reused for ten times with no obvious decrease in degradation efficiency of RhB, which could still reach 97% in the tenth run. The excellent durability of $\text{Ag}_3\text{PO}_4/\text{3DOM-WO}_3$ catalysts in the RhB degradation may be explained by the special transfer pathway of electrons and holes as described in Fig. 8. The photogenerated electrons were enriched on the surface of 3DOM-WO_3 instead of Ag_3PO_4 , which could effectively protect Ag_3PO_4 against corrosion ($\text{Ag}^+ + \text{e}^- \rightarrow \text{Ag}^0$). To further confirm the explanation of improved stability of $\text{Ag}_3\text{PO}_4/\text{3DOM-WO}_3$ catalysts, the used catalysts in RhB degradation were characterized by XPS.

Fig. 13 depicts the high-resolution Ag3d XPS spectra of Ag_3PO_4 used one time and A5W5(270) used one or ten times in RhB photodegradation. The $\text{Ag3d}_{5/2}$ and $\text{Ag3d}_{3/2}$ peaks near 368 and 374 eV could be fitted to two separate peaks corresponding to Ag^0 and Ag^+ ions [53,57–59]. It could be found that more than 27% of Ag^0 was formed on the surface of pure Ag_3PO_4 catalyst after one run, while only less than 5% of Ag^0 was detected on the surface of A5W5(270). Even after ten runs the molar content of Ag^0 on the surface of A5W5(270) was still less than 21%. Therefore, the $\text{Ag}_3\text{PO}_4/\text{3DOM-WO}_3$ catalysts exhibited excellent durability in the visible light photocatalytic degradation of organic contaminants.

3.7. Oxygen evolution performance of $\text{Ag}_3\text{PO}_4/\text{3DOM-WO}_3$ composites

The novel $\text{Ag}_3\text{PO}_4/\text{3DOM-WO}_3$ composites could be also used in the visible light photocatalytic water splitting for oxygen evolution. Fig. 14 shows the time courses of photocatalytic water oxidation on Ag_3PO_4 and A5W5(270) using AgNO_3 as an electron scavenger. It could be found that in the first hour pure Ag_3PO_4 exhibited slightly higher water oxidation activity compared with A5W5(270). After 2 h, however, the oxygen evolution was prevented due to the complete covering of Ag_3PO_4 surface with metallic Ag derived from the electron scavenger used in the experiment ($\text{Ag}^+ + \text{e}^- \rightarrow \text{Ag}^0$). The similar result was also reported by Martin et al. [60] While for the composite catalyst A5W5(270), notably enhanced durability was presented in the photocatalytic water oxidation. The amount of oxygen evolution over A5W5(270) was comparable to Ag_3PO_4 for 2 h, and significantly exceed Ag_3PO_4 after 3 h. The catalyst A5W5(270) was observed to be not deactivated until 5 h. Thus the total amount of oxygen evolution over A5W5(270) was notably higher than Ag_3PO_4 .

Fig. 15 shows the HRTEM images of used A5W5(270) in the water splitting experiment for 5 h. It could be found that the three-dimensionally ordered macroporous structure of A5W5(270) was well preserved, suggesting that the present composite catalyst was very stable during the reaction. Additionally, a large amount of metallic Ag nanoparticles were detected on the surface of 3DOM-WO_3 , which was derived from the electron scavenger of AgNO_3 . This provided a direct evidence to support the view that the photogenerated electrons were mainly enriched on the surface

of 3DOM-WO_3 . Thus the combination of Ag_3PO_4 and 3DOM-WO_3 can dramatically improve the durability of the photocatalyst.

4. Conclusions

In this work, novel $\text{Ag}_3\text{PO}_4/\text{3DOM-WO}_3$ photocatalysts were synthesized and employed in the visible light degradation of organic contaminants (including phenol, BPA, RhB, MB and MG) and water splitting for oxygen evolution. Compared with Ag_3PO_4 , 3DOM-WO_3 , $\text{Ag}_3\text{PO}_4/\text{Rod-WO}_3$ and $\text{Ag}_3\text{PO}_4/\text{Plate-WO}_3$, $\text{Ag}_3\text{PO}_4/\text{3DOM-WO}_3$ exhibited notably enhanced photocatalytic efficiency. This was mainly attributed to the synergic effect of Ag_3PO_4 and 3DOM-WO_3 as well as the periodic macroporous structure of 3DOM-WO_3 , which could lead to efficient electron-hole separation, convenient mass transfer and enhanced light energy conversion efficiency. The effects of $\text{Ag}_3\text{PO}_4:\text{WO}_3$ mass ratio and 3DOM-WO_3 pore diameter on the photocatalytic performance were studied and the slow photon effect in $\text{Ag}_3\text{PO}_4/\text{3DOM-WO}_3$ catalysts was demonstrated. When the stop band of 3DOM-WO_3 was exactly overlapped with the electronic absorption band of $\text{Ag}_3\text{PO}_4/\text{3DOM-WO}_3$ composite, the photocatalytic efficiency would be significantly enhanced. Moreover, owing to the special transfer pathway of electrons and holes, these composite photocatalysts were perfectly stable in the visible light degradation of organic contaminants and water splitting for oxygen evolution.

Acknowledgements

This work was supported by the National High Technology Research and Development Program of China (Grant no. 2012AA063008), the National Natural Science Foundation of China (Grant no. 21203102), the Tianjin Municipal Natural Science Foundation (Grant nos. 14JCQNJC06000 and 14JCZDJC32000) and MOE (IRT13R30).

Appendix A. Supplementary data

Supplementary data associated with this article can be found, in the online version, at <http://dx.doi.org/10.1016/j.apcatb.2015.04.017>.

References

- [1] H. Tong, S. Ouyang, Y. Bi, N. Umezawa, M. Oshikiri, J. Ye, *Adv. Mater.* 24 (2012) 229–251.
- [2] A. Kubacka, M. Fernández-García, G. Colón, *Chem. Rev.* 112 (2012) 1555–1614.
- [3] O.D. Velev, T.A. Jede, R.F. Lobo, A.M. Lenhoff, *Nature* 389 (1997) 447–448.
- [4] B.T. Holland, C.F. Blanford, A. Stein, *Science* 281 (1998) 538–540.
- [5] J.E.G.J. Wijnhoven, W.L. Vos, *Science* 281 (1998) 802–804.
- [6] Y.N. Xia, B. Gates, Y.D. Yin, Y. Lu, *Adv. Mater.* 12 (2000) 693–713.
- [7] O.D. Velev, A.M. Lenhoff, *Curr. Opin. Colloid Interface Sci.* 5 (2000) 56–63.
- [8] A. Stein, R.C. Schroden, *Curr. Opin. Solid State Mater. Sci.* 5 (2001) 553–564.
- [9] M. Srinivasarao, D. Collings, A. Philips, S. Patel, *Science* 292 (2001) 79–83.
- [10] A. Stein, B.E. Wilson, S.G. Rudisill, *Chem. Soc. Rev.* 42 (2013) 2763–2803.
- [11] S. Nishimura, N. Abrams, B.A. Lewis, L.I. Halaoui, T.E. Mallouk, K.D. Benckstein, J. van de Lagemaat, A.J. Frank, *J. Am. Chem. Soc.* 125 (2003) 6306–6310.
- [12] S.-H.A. Lee, N.M. Abrams, P.G. Hoertz, G.D. Barber, L.I. Halaoui, T.E. Mallouk, *J. Phys. Chem. B* 112 (2008) 14415–14421.
- [13] Y. Li, F. Piret, T. Léonard, B.-L. Su, *J. Colloid Interface Sci.* 348 (2010) 43–48.
- [14] M. Wu, Y. Li, Z. Deng, B.-L. Su, *ChemSusChem* 4 (2011) 1481–1488.
- [15] M. Wu, A. Zheng, F. Deng, B.-L. Su, *Appl. Catal. B: Environ.* 138–139 (2013) 219–228.
- [16] D. Qi, L. Lu, Z. Xi, L. Wang, J. Zhang, *Appl. Catal. B: Environ.* 160–161 (2014) 621–628.
- [17] J.L. Chen, G. von Freymann, S.Y. Choi, V. Kitaev, G.A. Ozin, *Adv. Mater.* 18 (2006) 1915–1919.
- [18] M. Srinivasan, T. White, *Environ. Sci. Technol.* 41 (2007) 4405–4409.
- [19] Q. Li, J.K. Shang, *J. Am. Ceram. Soc.* 91 (2008) 660–663.
- [20] J.L. Chen, G.A. Ozin, *J. Mater. Chem.* 19 (2009) 2675–2678.
- [21] J. Xu, B. Yang, M. Wu, Z. Fu, Y. Lv, Y. Zhao, *J. Phys. Chem. C* 114 (2010) 15251–15259.
- [22] F. Sordello, C. Duca, V. Maurino, C. Minero, *Chem. Commun.* 47 (2011) 6147–6149.

- [23] Y. Lu, H. Yu, S. Chen, X. Quan, H. Zhao, *Environ. Sci. Technol.* 46 (2012) 1724–1730.
- [24] F. Sordello, C. Minero, *Appl. Catal. B: Environ.* 163 (2015) 452–458.
- [25] S. Sun, W. Wang, L. Zhang, *J. Mater. Chem.* 22 (2012) 19244–19249.
- [26] Y. Wang, H. Dai, J. Deng, Y. Liu, H. Arandiyán, X. Li, B. Gao, S. Xie, *Solid State Sci.* 24 (2013) 62–70.
- [27] Y. Wang, H. Dai, J. Deng, Y. Liu, Z. Zhao, X. Li, H. Arandiyán, *Chem. Eng. J.* 226 (2013) 87–94.
- [28] K. Ji, J. Deng, H. Zang, J. Han, H. Arandiyán, H. Dai, *Appl. Catal. B: Environ.* 165 (2015) 285–295.
- [29] M. Sadakane, K. Sasaki, H. Kunioku, B. Ohtani, R. Abe, W. Ueda, *J. Mater. Chem.* 20 (2010) 1811–1818.
- [30] X. Chen, J. Ye, S. Ouyang, T. Kako, Z. Li, Z. Zou, *ACS Nano* 5 (2011) 4310–4318.
- [31] L. Zhang, C.-Y. Lin, V.K. Valev, E. Reisner, U. Steiner, J.J. Baumberg, *Small* 10 (2014) 3970–3978.
- [32] K. Ji, H. Dai, J. Deng, H. Zang, H. Arandiyán, S. Xie, H. Yang, *Appl. Catal. B: Environ.* 168–169 (2015) 274–282.
- [33] S.-L. Chen, A.-J. Wang, C. Dai, J.B. Benziger, X.-C. Liu, *Chem. Eng. J.* 249 (2014) 48–53.
- [34] L. Chen, L. Xie, M. Wang, X. Ge, *J. Mater. Chem. A* 3 (2015) 2991–2998.
- [35] Z. Yi, J. Ye, N. Kikugawa, T. Kako, S. Ouyang, H. Stuart-Williams, H. Yang, J. Cao, W. Luo, Z. Li, Y. Liu, R.L. Withers, *Nat. Mater.* 9 (2010) 559–564.
- [36] Y. Bi, S. Ouyang, N. Umezawa, J. Cao, J. Ye, *J. Am. Chem. Soc.* 133 (2011) 6490–6492.
- [37] H. Katsumata, M. Taniguchi, S. Kaneco, T. Suzuki, *Catal. Commun.* 34 (2013) 30–34.
- [38] J. Ma, J. Zou, L. Li, C. Yao, T. Zhang, D. Li, *Appl. Catal. B: Environ.* 134–135 (2013) 1–6.
- [39] W. Teng, X. Li, Q. Zhao, J. Zhao, D. Zhang, *Appl. Catal. B: Environ.* 125 (2012) 538–545.
- [40] H. Yu, G. Cao, F. Chen, X. Wang, J. Yu, M. Lei, *Appl. Catal. B: Environ.* 160–161 (2014) 658–665.
- [41] S. Zhang, S. Zhang, L. Song, *Appl. Catal. B: Environ.* 152–153 (2014) 129–139.
- [42] Q. Xiang, D. Lang, T. Shen, F. Liu, *Appl. Catal. B: Environ.* 162 (2015) 196–203.
- [43] X. Ma, H. Li, Y. Wang, H. Li, B. Liu, S. Yin, T. Sato, *Appl. Catal. B: Environ.* 158–159 (2014) 314–320.
- [44] C. Cui, Y. Wang, D. Liang, W. Cui, H. Hu, B. Lu, S. Xu, X. Li, C. Wang, Y. Yang, *Appl. Catal. B: Environ.* 158–159 (2014) 150–160.
- [45] P. Dong, Y. Wang, B. Cao, S. Xin, L. Guo, J. Zhang, F. Li, *Appl. Catal. B: Environ.* 132–133 (2013) 45–53.
- [46] S. Kumar, T. Surendar, A. Baruah, V. Shanker, *J. Mater. Chem. A* 1 (2013) 5333–5340.
- [47] Y.-S. Xu, W.-D. Zhang, *Dalton Trans.* 42 (2013) 1094–1101.
- [48] J. Kim, C.W. Lee, W. Choi, *Environ. Sci. Technol.* 44 (2010) 6849–6854.
- [49] B.J.S. Johnson, A. Stein, *Inorg. Chem.* 40 (2001) 801–808.
- [50] J. Du, X. Lai, N. Yang, J. Zhai, D. Kisailus, F. Su, D. Wang, L. Jiang, *ACS Nano* 5 (2011) 590–596.
- [51] M. Ren, R. Ravikrishna, K.T. Valsaraj, *Environ. Sci. Technol.* 40 (2006) 7029–7033.
- [52] L. Liu, J. Liu, D.D. Sun, *Catal. Sci. Technol.* 2 (2012) 2525–2532.
- [53] Y. Liu, L. Fang, H. Lu, Y. Li, C. Hu, H. Yu, *Appl. Catal. B: Environ.* 115–116 (2012) 245–252.
- [54] G. Fu, G. Xu, S. Chen, L. Lei, M. Zhang, *Catal. Commun.* 40 (2013) 120–124.
- [55] W.-C. Peng, X. Wang, X.-Y. Li, *Nanoscale* 6 (2014) 8311–8317.
- [56] Y.P. Xie, G.S. Wang, *J. Colloid. Interface Sci.* 430 (2014) 1–5.
- [57] H. Lin, H. Ye, B. Xu, J. Cao, S. Chen, *Catal. Commun.* 37 (2013) 55–59.
- [58] J. Cao, B. Luo, H. Lin, B. Xu, S. Chen, *J. Hazard. Mater.* 217–218 (2012) 107–115.
- [59] J. Zhang, K. Yu, Y. Yu, L.-L. Lou, Z. Yang, J. Yang, S. Liu, *J. Mol. Catal. A: Chem.* 391 (2014) 12–18.
- [60] D.J. Martin, N. Umezawa, X. Chen, J. Ye, J. Tang, *Energy Environ. Sci.* 6 (2013) 3380–3386.